Metrol. Meas. Syst., Vol. 29 (2022) No. 2, pp. 347–360
DOI: 10.24425/mms.2022.140037

PAN POLSKA AKADEMIA NAUK

METROLOGY AND MEASUREMENT SYSTEMS
Index 330930, ISSN 0860-8229
www.metrology.wat.edu.pl

M&MS

SURFACE DAMAGE ASSESSMENT BY ANALYSIS OF ELECTRICAL RESISTANCE CHANGES IN GRAPHITE-BASED SENSING SKIN

Marek Stepnowski[1)], Daniel Janczak[2)], Małgorzata Jakubowska[2)], Paweł Pyrzanowski[1)]

1) *Warsaw University of Technology, Institute of Aeronautics and Applied Mechanics, Nowowiejska 24, 00-665 Warsaw, Poland* (✉ *marek.stepnowski.dokt@pw.edu.pl*, +48 22 234 52 11, *pawel.pyrzanowski@pw.edu.pl*)
2) *Warsaw University of Technology, Institute of Metrology and Biomedical Engineering, Św. Andrzeja Boboli 8, 02-525 Warsaw, Poland* (*d.janczak@mchtr.pw.edu.pl*, *m.jakubowska@mchtr.pw.edu.pl*)

Abstract

The article presents the method of identifying surface damage by measuring changes in resistance in graphite-based sensing skin. The research focused on analysis of conductivity anomalies caused by surface damage. Sensitivity maps obtained with Finite Element Method (FEM) in conjunction with the analytical damage model were used to build the coating evaluation algorithm. The experiment confirmed the ability of this method to identify a single elliptical-shape damage. Eight electrodes were enough to locate the damage that covered about 0.1‰ of the examined area. The proposed algorithm can prove useful in simple applications for surface condition monitoring. It can be implemented wherever it is possible to apply a thin layer of conductor to a non-conductive surface.

Keywords: sensing skin, damage, detection, algorithm, ERT.

1. Introduction

Self-sensing materials have enormous potential to improve human and structural safety. Contrary to traditional point sensors, where only sensory information is recorded in the immediate vicinity of the sensor, the self-sensing material is the sensor itself and every part of it is capable of relaying sensory information. These types of materials are especially attractive for *Structural Health Monitoring* (SHM) because they allow to reduce the burden associated with the implementation of dense grids of point sensors. A common approach to self-detection is response to stimuli obstructing the flow of electric current because electrical measurements are quick and easy to take. *Electrical Impedance Tomography* (EIT) has huge potential in this area. EIT methods are widely used due to their harmlessness and non-invasiveness and they found applications in medicine [1], geological research [2] and process engineering [3]. There is also visible growing popularity of EIT in structural health and condition monitoring [4–6]. Many studies are

Article history: received December 11, 2021; revised January 31, 2022; accepted March 5, 2022; available online April 22, 2022.

focused on application of EIT methods in carbon composites including *Carbon-Fibre-Reinforced Polymers* (CFRPs). Some of the studies are presented in papers [7–9]. However, when the entire high conductance structure is tested, a low value of resistance means that small currents must be measured. Even when a four-wire resistance measurement method is used, the measurements are subject to a large error due to a very high level of noise [10]. The method is also not effective for non-conductive materials such as glass composites or dried concrete. The solution can be a conductive layer with specially designed conductivity applied to the surface of a non-conductive object called the sensing skin. To apply it on conductive objects, an insulating layer is also needed. Hallaji *et al*. developed a sensing skin consisting of a thin layer of electrically conductive copper paint that is applied to the surface of concrete in order to image cracks [11]. Similar studies using carbon-filled coatings were conducted by Dai with a carbon nanotube-based composite sensor [12]. Tallman showed promising SHM results using EIT in thin carbon-based epoxy resin [13]. Loh, K. J.'s team have also performed extensive work on thin film sensors for SHM application [14, 15]. It should be mentioned here that sensing skin can be applied to non-planar surfaces as Jauhiainen *et al.* did [16]. Very good results in visualizing cracks using sensing skin were also shown by Smyl *et al*. [17]. In recent years, a lot of research has been conducted in this field. Only some of the works related to the EIT with the use of sensing skin are cited. The closest competitor of the EIT methods applied in sensitive skin are the methods of interpolated resistance change. Interpolated resistance change methods identify and localize stimuli in self-sensing materials via simple $V = IR$ measurements collected over the surface of the domain or through its thickness [18–20]. The chief advantage of interpolated change methods is that they are computationally low-cost and very simple to implement. However, they also suffer from important limitations *i.e*., they require extremely high numbers of electrodes to localize conductivity-changing effects. And even with many electrodes, the shaping is poor. The most cited argument against the EIT is that it is computationally expensive. However, the benefits of the fewer electrodes and better accuracy speak for the EIT [21].

In summary, the EIT is a powerful tool for visualizing the distribution of electrical properties in the observed area, which has many applications. One of them is the detection of damage in sensitive skin, which has been intensively studied in recent years. Also, many examples of sensors using carbon were described in papers [22, 23]. The electrical properties of the sensing skin can be adjusted by the amount of the carbon filler and by the thickness of the applied layer [24]. A thin sensitive skin with relatively high resistivity can be used to improve the quality of the two-lead measurements method [25]. In addition, in sensitive skins applications, we are often not directly interested in the distribution of resistance, but only in information about the cause of the changes – *e.g*., information about damage. This article shows a new approach to the problem of relating the measured resistance changes to coating damage parameters. The expected failure type was parametrically modeled in order to relate the failure parameters to the measured changes in resistance. The analytical model of a single failure was used in conjunction with the area sensitivity maps obtained by the FEM model.

In the presented case, the expected damage is an ellipse-shaped defect. Depending on the damage parameters, it can be a circle, an ellipse or a thin slit. Similarly shaped damage may arise from impacts, scratches or cracks at an early stage. The distribution of the coating resistivity is homogeneous and known. The resistivity of the applied coating must be measured and the proposed algorithm should be calibrated to the coating applied. Contrary to the popular EIT methods, the distribution of physical properties of the studied area (*e.g*., conductivity) is not calculated so there is no need to solve the inverse problem (conductivity distribution).

Metrol. Meas. Syst., Vol. 29 (2022), No. 2, pp. 347–360
DOI: 10.24425/mms.2022.140037

2. Materials and methodology

2.1. General methodology

General measurement methodology is presented in Fig. 1a. The electrodes are placed at the boundary of the conductive layer. The two-wire method is used to measure the resistance of studied coating. The actual measured value – R_m is described in (1)

$$R_m = R_{\text{coating}} + R_{\text{contact}}\,, \tag{1}$$

where R_{coating} is resistance of the graphite coating and R_{contact} is resistance of the contacts and wires. The problem consists in linking the registered resistance changes with the damage parameters. The algorithm solving this problem could be used in the structure monitoring system whose the architecture is shown in Fig. 1b.

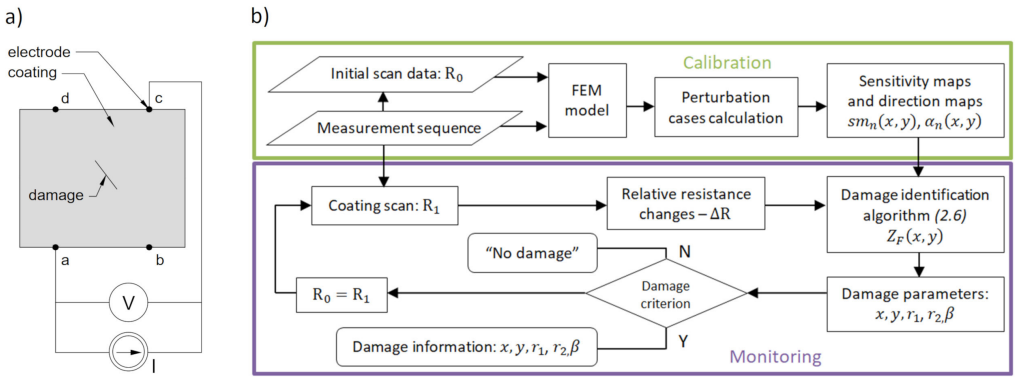

Fig. 1. General methodology: a) of measurements, b) of the proposed monitoring system.

Measurement is performed in steady state. It is necessary to solve the forward problem in order to compare the state with and without damage. By neglecting the magnetic field when using static currents, Faraday's law of induction and Ampere's law can be combined to yield (2) as Loh, K. J. *et al.* showed in [26]

$$\nabla \cdot (\sigma \nabla \phi(x, y)) = 0, \quad x, y \in A, \tag{2}$$

where ϕ is electric potential, σ is conductivity of the undamaged coating bounded by area A. Here it is assumed that current is neither supplied nor generated within the coating, hence the right side of the equation is set to zero. The flow of a current within the body is therefore due to the current supplied at the boundary of coating. Moreover, σ is constant. Equation (2) leads to Laplace's equation. It is assumed that no current flows through the damage so the damaged area is excluded from the domain. It is complicated to find an analytical solution to Laplace's equation with the boundary conditions as shown in Fig. 1a. In turn, linking the damage parameters (such as size, shape, position, orientation) with the registered resistance changes only with the FEM model requires data for a huge number of cases. The problem was divided into two stages assuming that the expected damage would be much smaller than the examined area. The first stage consists in the analytical determination of the qualitative influence of the damage shape and orientation on the change of the homogeneous potential field. In the second stage, the global solution for a circular-shape damage coating was developed using the FEM model.

2.2. Mathematical model of single damage in a uniform potential field

The combination of solutions of elementary potential flows: X direction flow + dipole leads to a solution for potential flow around a circle with radius r. Using complex variables and complex functions, the stream function – ψ and potential – ϕ can be recast in terms of a single complex function $w(z)$ (3). The real part of $w(z)$ describes the potential field, and the imaginary part describes the streamlines. A detailed description of the derivation $w(z)$ is described in [27]

$$w(z) = U_\infty \left(z + \frac{r^2}{z} \right) = \phi + i\psi. \tag{3}$$

Using $z = x + iy$ we find potential field in Cartesian coordinates:

$$\phi = U_\infty \left(x + \frac{xr^2}{x^2 + y^2} \right). \tag{4}$$

The damage impact on the voltage – ΔU between measurement points $z_1(l, 0)$, $z_2(-l, 0)$ can be described as the difference of voltages in the cases with damage – U_1 and without damage – U_2 (5) respectively

$$\Delta U = U_1 - U_2 = [\phi_1(z_1) - \phi_1(z_2)] - [\phi_2(z_1) - \phi_2(z_2)], \tag{5}$$

where ϕ_1, ϕ_2 are the values of the potential ϕ in the cases with ($r \neq 0$) and without ($r = 0$) failure, respectively. Both are determined using (4). Applying (4) to (5) leads to the formula for the voltage change between the measurement points caused by a circular failure (6)

$$\Delta U = 2U_\infty \frac{r^2}{l}. \tag{6}$$

A solution for more complicated shapes of damage can be achieved by conformal mapping. In this case, solution (3) was modified with the Joukovsky transformation (7) to obtain a solution for the flow around the ellipse (8)

$$z = \zeta + \frac{c^2}{\zeta}, \tag{7}$$

$$w(z) = U_\infty \left(\zeta e^{-i\alpha} + \frac{r^2}{\zeta} e^{i\alpha} \right) = \phi + i\psi, \tag{8}$$

where, α describes the flow direction and coefficients r and c define the shape proportions of the ellipse with semi-major axis (r_1) and semi-minor axis (r_2). Solution (8) was used to find the influence of damage parameters on voltage changes in accordance with (5). The analytical determination of ϕ is quite messy. A discrete method was used. The distance between the measurement points z_1, $z_2 = -z_1$ was greater than the characteristic size of damage – r_1. The effect of ellipse-shaped damage (ΔU_D) with dimension $r_1 = 1$ compared to the effect of damage in the shape of a circle (ΔU_0) with radius $r_1 = r_2 = 1$ is shown in Fig. 2b. Since the ratio of changes is analyzed, it does not matter if the changes are relative or absolute. Figure 2c shows the relationship between the shape ratio and the relative voltage change in the two extreme cases of angle α. For the $\alpha = 0°$ a linear relationship was observed and approximated by (9).

$$\frac{\max(\Delta U_D)}{\Delta U_0} = 0.5 \cdot \left(\frac{r_2}{r_1} + 1 \right). \tag{9}$$

Metrol. Meas. Syst., Vol. 29 (2022), No. 2, pp. 347–360
DOI: 10.24425/mms.2022.140037

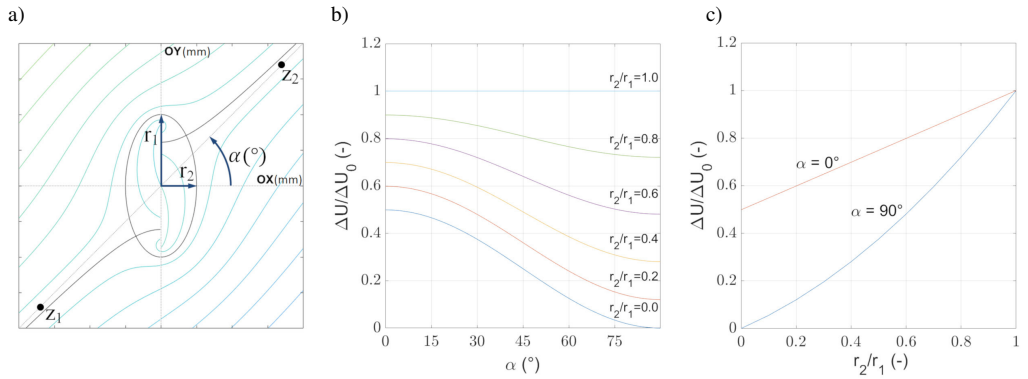

Fig. 2. Analytical results: a) Stream lines of the flow around ellipse-shaped ($\boldsymbol{r_1}$, $\boldsymbol{r_2}$) damage. $\boldsymbol{\Delta U}$ in relation to the circular fault effect $\boldsymbol{\Delta U_0}$ in: b) flow direction – $\boldsymbol{r_2/r_1}$.

In the case of a circle, the flow direction has no effect on the value of the observed voltage change, which was expected. The slenderer the shape of the ellipse, the greater the influence of the flow angle on the voltage change. It can be observed that, due to the elliptical failure the voltage change, is dependent on the α similar as $\cos(\alpha)$ function. Furthermore, the following correlation was observed (10)

$$\frac{r_2}{r_1} \approx \frac{\min(\Delta U)}{\max(\Delta U)}\,. \tag{10}$$

A model of the angular resistance characteristic $\overline{R}_D$ (11) was built using Ohm's law and solution of the potential field from (8). This model relates the resistances caused by elliptical ($r_1 r_2$) failure – $\Delta R_D(\alpha)$, to the resistances caused by a circular ($r = r_1$) failure – ΔR_{otsr} or circular ($r = r_0$) failure – ΔR_0

$$\overline{R}_D\,(\alpha+\beta) = \frac{\Delta R_D(\alpha)}{\Delta R_{\text{otsr}}} \cdot s^2 = \frac{\Delta R_D(\alpha)}{\Delta R_o} = s^2 \cdot \left[C_1 \cdot \cos\left(2\,(\alpha+\beta)\right) + C_2\right]. \tag{11}$$

Factors C_1 and C_2 describe the cosine curve and s is the scale factor relating ΔR_{otsr} and ΔR_o according to Formula (12). β is the angle corresponding to the damage orientation in the coating coordinate system and it is used in Section 2.6. The set of equations (12)–(14) was determined using Ohm's law and (6), (9) and (10).

$$\frac{\Delta R_{\text{otsr}}}{\Delta R_o} = \left(\frac{r_1}{r_0}\right)^2 = s^2, \tag{12}$$

$$\frac{\max\left(\overline{R}\right)}{\Delta R_{\text{otsr}}} = 0.5 \cdot \left(\frac{r_2}{r_1} + 1\right), \tag{13}$$

$$\frac{r_2}{r_1} \approx \frac{\min\left(\overline{R}_D\right)}{\max\left(\overline{R}_D\right)}\,. \tag{14}$$

From the set of (12)–(14) the scale factor can be calculated as (15).

$$s = \sqrt{2 \cdot \frac{\max\left(\overline{R}_D\right)}{\Delta R_o} \cdot \left(\frac{\min\left(\overline{R}_D\right)}{\max\left(\overline{R}_D\right)} + 1\right)^{-1}}. \tag{15}$$

Semi axes r_1 and r_2 of the ellipse are described by (16) and (17)

$$r_1 = r_0 \cdot s, \tag{16}$$

$$r_2 = r_1 \cdot \frac{\min\left(\overline{R}_D\right)}{\max\left(\overline{R}_D\right)}. \tag{17}$$

It is worth noting that all the data needed to solve (16) and (17) can be achieved from the characteristics $\overline{R}_D$ (11) using (18) and (19)

$$\frac{\min\left(\overline{R}_D\right)}{\max\left(\overline{R}_D\right)} = \frac{C_2 - |C_1|}{C_2 + |C_1|}, \tag{18}$$

$$\frac{\max\left(\overline{R}_D\right)}{\Delta R_o} = C_2 + |C_1|. \tag{19}$$

The construction of the $\overline{R}_D$ characteristic, apart from the results of resistance measurements, requires information about the system's response to the reference circular ($r = r_0$) failure which is described in Section 2.5.

2.3. Specimen preparation and Data Acquisition System (DAS)

The experiment was performed on a square-shaped (50 mm × 50 mm) conductive coating. The tested samples were prepared from silver- and carbon-based polymer composites by screen-printing using an AUREL Mod. C902 printer. A Loctite EDAG 725A paste was applied to a polycarbonate film to prepare contact electrodes (thickness about 12 µm). After drying the conductive layer for 15 minutes at 130°C, a carbon layer was applied. Carbon coating was made of a polymer composite containing the functional phase a mixture of graphite micro-flakes (particle diameter < 25 µm) and carbon black (particle size 30 nm, surface area 250 m^2/g). The composition of the paste based on the polymer carrier of Novelinks (PL) contained 25 wt.% filler with the 50:50 ratio. The second layer was cured in the same way. The measured sheet resistivity of the produced carbon coating was $\rho_s = 6.4\ \Omega$. The specimen design and photos are shown in Fig. 3.

The built DAS allows a two-wire scan using up to 72 electrodes, 18 at each edge, spaced 2.54 mm apart so a standard edge connector can be used to connect the specimen to the measurement system. To ensure the greatest possible versatility of the specimen, the maximum possible number of electrodes were placed on the specimen, which is relatively easy with the used screen-printing technology. The proposed method uses only $e = 8$ electrodes marked in the scheme in Fig. 3a, which allows selection of $N = 28$ different pairs of electrodes according to (20)

$$N = \frac{e \cdot (e-1)}{2}. \tag{20}$$

Metrol. Meas. Syst., Vol. 29 (2022), No. 2, pp. 347–360
DOI: 10.24425/mms.2022.140037

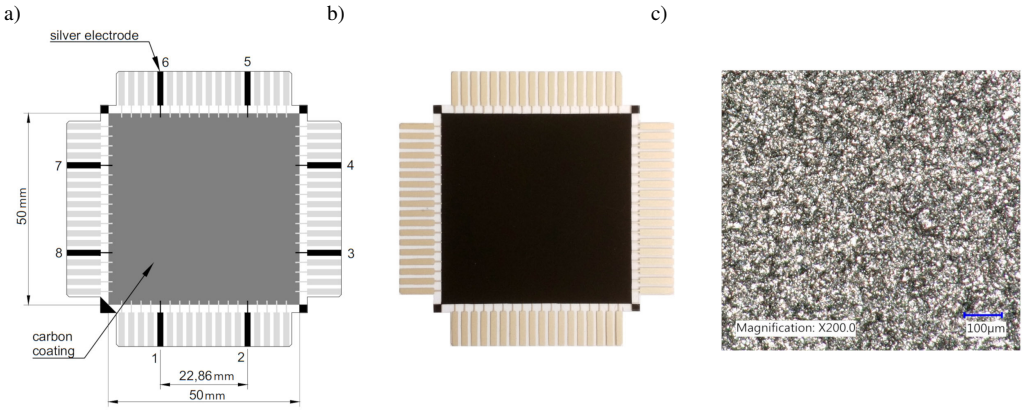

Fig. 3. a) Specimen design with active electrodes marked, b) Specimen photography, c) Microscope photography of graphite coating.

A block diagram of the DAS is shown in Fig. 4. Its main components are a reed switch-based analogue multiplexer, a specimen connected to the measuring circuit through the multiplexer, a high precision voltage source, a resistor, an analogue-digital converter, a microprocessor and a PC. The two-wire resistance measurement is performed after connecting the specimen to the measurement circuit with the selected pair of electrodes. The sample scan provides a dataset of 28 measurements to determine the resistance in different directions. The influence of the temperature change was negligible due to the short scanning time.

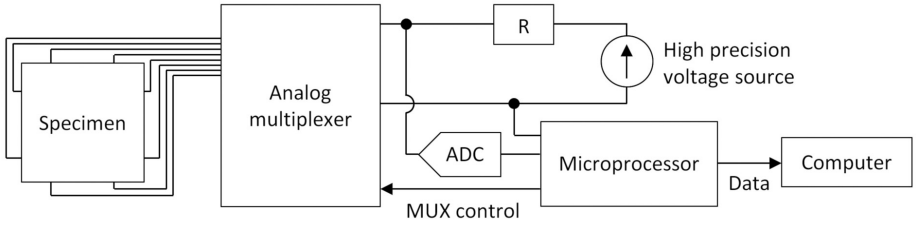

Fig. 4. Block diagram of the DAS.

2.4. FEM investigation

A 2D FEM model of the studied coating was built to solve the forward problem (2) with boundary condition (21)

$$\nabla\phi(x,y)\cdot\vec{n} = g(x,y), \quad x,y \in \partial A, \tag{21}$$

where $\vec{n}$ is a unit vector pointing to the outside of the coating area and $g(x,y)$ is a function that describes the current flow across the boundary of the studied area. The FEM model was built using the Ansys APDL code. The isotropic material was modelled using PLANE230 elements whose nodes have only one degree of freedom *i.e.*, the electric potential. The analysis consists in forcing a constant current – I_{FEM} through the pair of electrodes nodes. The results are electric potential distribution and its derivatives. Exemplary results of current density distribution are shown in Fig. 5.

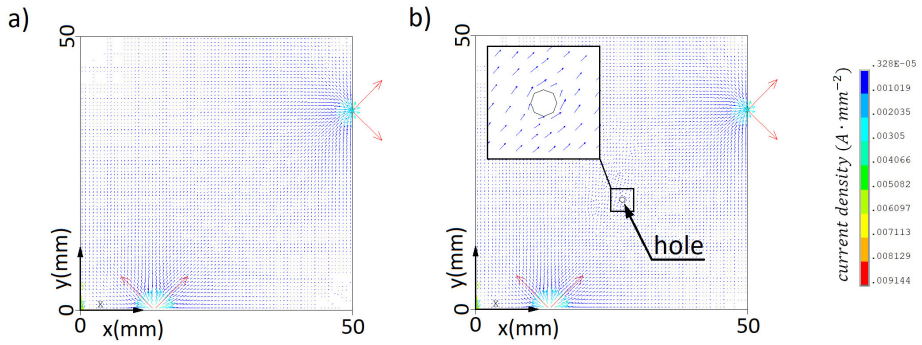

Fig. 5. Vector plot of current density: a) Undamaged coating. b) Coating with 1 mm diameter hole.

The FEM model also allows to export voltage value between the n-pair of sources nodes – $U_{\mathrm{FEM},n}$. Ansys uses the *Reduced Scalar Potential* (RSP) strategy described by Zienkiewicz [28]. It leads to a finite value of the potential in the source node by calculating the Biot–Savart integral over the neighbourhood of source. In this case the Biot–Savart integral is valid assuming that there is no iron within the problem domain. The boundary of the Biot–Savart integral has a significant influence on the value of voltage. The integral boundary depends on the finite element size, so the size of the elements near the edge of the coating area were fixed when the mesh was modified. It is important that the FEM model, which is used to determine the sensitivity maps, gives correct quantitative and qualitative results that are needed for the proposed detection method. The actual contact resistance can be considered after the calibration of the FEM model according to (22) and (23).

$$R_{\mathrm{corr},n} = \frac{U_{\mathrm{FEM},n}}{I_{\mathrm{FEM}}} - R_c \,, \tag{22}$$

where, $R_{\mathrm{corr},n}$ is corrected resistance, R_c is constant resistance which in combination with the RSP strategy includes the actual contact resistance. R_c was found by minimizing the sum of errors (23).

$$\sum_{n=1}^{N} \left| R_{\mathrm{corr},n} - R_{\mathrm{exp},n} \right| = \sum_{n=1}^{N} \left| \frac{U_{\mathrm{FEM},n}}{I_{\mathrm{FEM}}} - R_c - R_{\mathrm{exp},n} \right| , \tag{23}$$

where, $R_{\mathrm{exp},n}$ is experimental measured resistance. The comparison of the corrected FEM data and the experimental data is presented in Fig. 6.

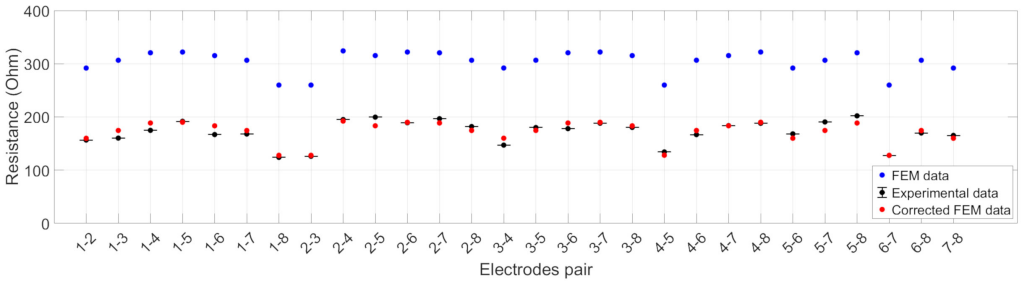

Fig. 6. Comparison of experimental and FEM results for undamaged coating.

Metrol. Meas. Syst., Vol. 29 (2022), No. 2, pp. 347–360
DOI: 10.24425/mms.2022.140037

As shown in the diagram (Fig. 6), the resistance values calculated with the FEM model with the default contact resistance settings are significantly different from the experimental data. The calibration method described with (22) and (23) provides a much better, though not perfect, compliance of the FEM model with the measured data. The differences in the results may be due to uneven resistivity distribution, different values of contact resistances in individual electrodes, different length of the wires or resistivity measurement error. It is worth emphasizing here that the differences between FEM data and experimental data do not correspond to the actual contact resistance. The actual contact resistance has been included but not calculated directly.

2.5. Sensitivity maps

The FEM model can be used to find the relative changes in resistance caused by circular damage – δ_n (24).

$$\delta_n = \frac{R_{1,\mathrm{corr},n} - R_{0,\mathrm{corr},n}}{R_{0,\mathrm{corr},n}}, \tag{24}$$

where, $R_{0,\mathrm{corr},n}$ is a corrected resistance value for undamaged coating and $R_{1,\mathrm{corr},n}$ is the corresponding value for the damaged coating. A set of simulations was performed to construct a relationship between the damage position and resistance changes. In each case a damage area with a diameter of $2r = 2r_0 = 1$ mm was simulated. The damage locations are shown in Fig. 7 (a). For each pair of electrodes, a matrix of values of changes in resistance was obtained, assigning the change to the location of the damage. For example, the results for the 3–6 pair are shown in Fig. 7b. Every bar corresponds to the results of one case simulation. Based on these results, 28 sensitivity matrices for all electrodes pairs were constructed. These matrices were interpolated over the higher density mesh to create sensitivity maps – $\delta_n(x, y)$. A sample sensitivity map is presented in Fig. 7c.

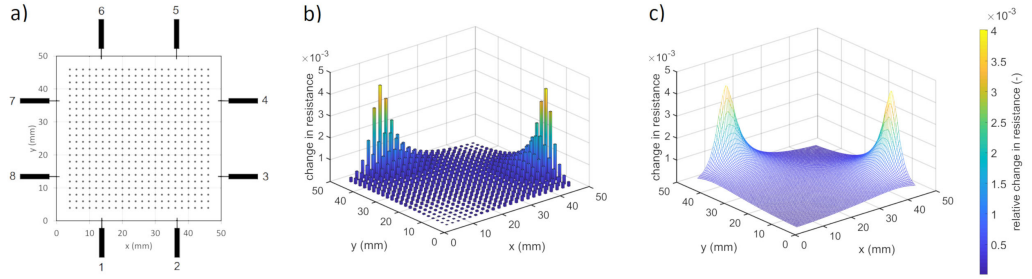

Fig. 7. Sensitivity map for electrode pair 3–6. a) Locations of perturbation points; b) Relative change in resistance as a function of damage position; c) Interpolated sensitivity map – $\boldsymbol{\delta_n}$ $\boldsymbol{(x,y)}$.

The FEM model was also used to find out the potential field gradient in the undamaged layer. Based on these results, direction maps – $\alpha_n(x, y)$ were constructed for each pair of electrodes. Direction maps are functions that assign to the points of the tested layer an angular value with which to describe the direction of undisturbed flow.

2.6. Damage identification algorithm

The damage identification algorithm combines the analytically obtained relationships between the damage model and circular damage with the sensitivity and direction maps obtained as a result

of the FEM simulation. The algorithm fits the damage model $\overline{R}_D$ (11) in the mesh nodes of the analyzed area and then assesses the quality of the fit. However, first the input data in the form of a set of measured resistances from two successive scans $R_0\,[1 \times n]$ and $R_1\,[1 \times n]$ are used to determine relative changes in resistance on successive pairs of electrodes – ΔR_n (25)

$$\Delta R_n = \frac{R_{1,n} - R_{0,n}}{R_{0,n}}\,. \tag{25}$$

At each mesh node $R_D\,[1 \times n]$ is determined with (26) to obtain the data set $(R_{D,n}, \alpha_n)$ that was used to fit the damage model $\overline{R}_D$.

$$R_{D,n} = \frac{\Delta R_n}{\delta_n}\,. \tag{26}$$

The Non-linear Least Squares (NLS) method is used to calculate C_1, C_2 and β. The assessment of the fit of the model to the measurement data is performed using the *Residual Sum of Squares* (RSS). RSS is used to build a model fit map – Z_F according to (27).

$$Z_F(x, y) = \frac{1}{\mathrm{RSS}}\,. \tag{27}$$

The maximum of the Z_F function indicates the location (x_{sA}, y_{sA}) where the damage model fit is the best, being the damage location criterion. Based on the fitted $\overline{R}_D$ model, the remaining damage parameters are calculated. The damage orientation in the global coordinate system – β can be found through (28).

$$\beta = \arg\max\left(\overline{R}_D\right). \tag{28}$$

Formulas (16–17) and (29–30) are used to find out length l_{1A} and width l_{2A} of damage.

$$l_{1A} = 2 \cdot r_1\,, \tag{29}$$

$$l_{2A} = 2 \cdot r_2\,. \tag{30}$$

The resolution and range of the Z_F map depends on the resolution and range of the sensitivity and directional maps. The damage identification algorithm was implemented using the MATLAB code. An example of the algorithm's results obtained on the FEM data is shown in Fig. 8.

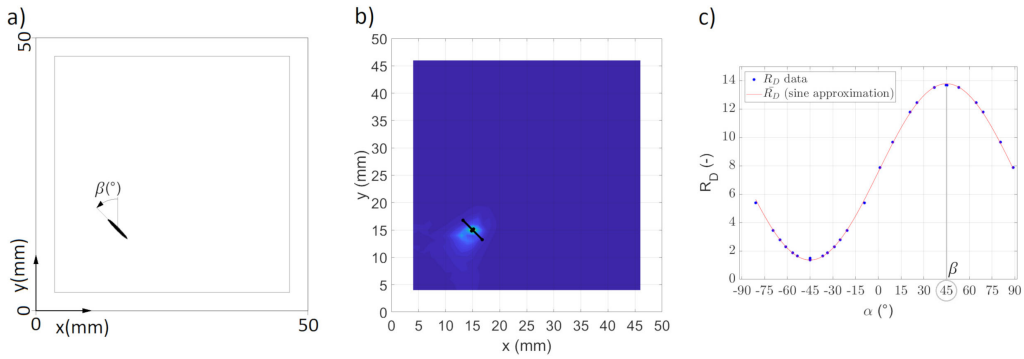

Fig. 8. Algorithm results for FEM data: a) Model of damaged specimen; b) $\boldsymbol{Z_F}$ graph with approximate dimensions of detected damage; c) $\boldsymbol{\overline{R}_D}$ characteristics at the damage location (x_{sA}, y_{sA}).

Metrol. Meas. Syst., Vol. 29 (2022), No. 2, pp. 347–360
DOI: 10.24425/mms.2022.140037

3. Experimental results

The system described in Section 2.3 was launched to monitor the condition of the prepared specimen. The specimen was damaged by making a cut and then enlarging it with a blade. A specimen scan was performed of the undamaged coating and each time after the damage was increased. The results of the algorithm operations are shown in Fig. 9. Row (I) shows results for the initial crack of about 0.8 mm in length which was gradually enlarged to 4.1 mm (row IV). There is a visible relationship between the accuracy of the indication and the size of the damage, which can be associated with high noise and measurement errors. However, in all cases indication of the damage was clear.

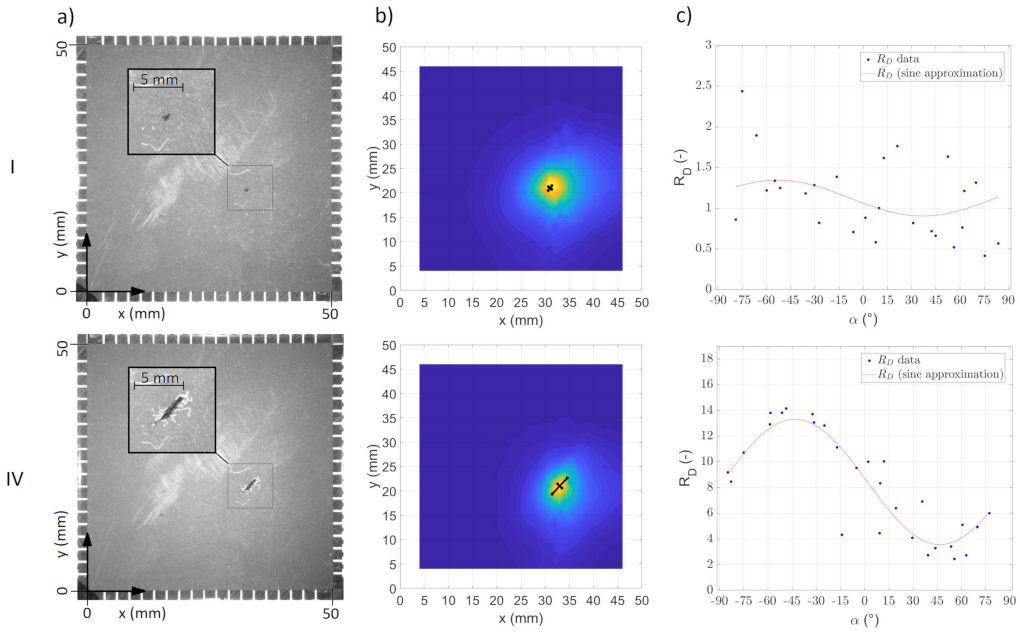

Fig. 9. Algorithm results for experimental data. a) Photographs of damaged specimen; b) $\boldsymbol{Z_F}$ graphs with designated dimensions of the detected damage; c) $\overline{\boldsymbol{R}}_{\boldsymbol{D}}$ characteristics in the extremes of the $\boldsymbol{Z_F}$ function.

The comparison of the data provided by the algorithm $(x_{sA}, y_{sA}, l_{1A}, l_{2A})$ with the experimental data $(x_{sE}, y_{sE}, l_{1E}, l_{2E})$ is presented in the Table 1. The coordinates of the center of damage

Table 1. Comparison of experimental and algorithm results.

Parameter	Experiment data				Algorithm data				Error				
	I	II	III	IV	I	II	III	IV	Definition	I	II	III	IV
x_s (mm)	20.6	20.7	20.9	21.2	21.3	21.5	20.9	20.9	$\lvert x_{sE} - x_{sA}\rvert/50$ mm	1.4%	1.6%	0,0%	0,6%
y_s (mm)	32.5	32.7	32.7	33.1	31.1	30.8	31.6	32.9	$\lvert y_{sE} - y_{sA}\rvert/50$ mm	2.8%	3.8%	2.2%	0.4%
l_1 (mm)	0.78	1.12	2.91	4.1	1.27	1.64	2.55	4.57	$\lvert l_{1E} - l_{1A}\rvert/l_{1E}$	62.8%	46.4%	12.4%	11.4%
l_2 (mm)	0.45	0.52	0.65	0.7	0.83	0.53	0.78	1.24	$\lvert l_{2E} - l_{2A}\rvert/l_{2E}$	84.4%	1.9%	20.0%	77.1%
α (°)	47	46	47	47	50	47	45	47	$\lvert \alpha_E - \alpha_A\rvert$	3°	1°	2°	0°

were found with an error not exceeding 4%. The obtained parameters of the size of the damage are characterized by a much greater error, up to 85%. The parameters of the damage were measured on the photos of the sample using a graphics program.

4. Conclusions

The presented simple method of identifying carbon coating damage allows for the description of localization and shape of a single damage area. The algorithm fits the damage model to the measured data. The method is based on anomaly analysis and it already has many limitations in relation to the classic EIT methods. For example, the limit of only one failure detection in the period between measurements. However, a relatively small number of electrodes combined with a simple, low-cost algorithm can be an interesting alternative to the currently used methods. The approximation (10) adopted in the model is correct if the distance between the damage and the electrode is greater than the size of the damage. As a consequence, the area close to the electrodes was excluded from the study. The applied ellipse-shaped model of damage can be useful in identifying damage areas in the form of cuts as shown in the experiment. Relatively good results were obtained in determining the location of the damage (error $< 4\%$). A relatively large error in determining the size of the damage may result from the differences between the actual shape of the damage and the shape adopted in the damage model. The use of alternative damage models seems to be an interesting continuation of this research.

References

[1] de Castro Martins, T., Sato, A. K., de Moura, F. S., de Camargo, E. D. L. B., Silva, O. L., Santos, T. B. R., Zhao, Z., Möeller, K., Amato, M. B. P., Mueller, J. L., Lima, R. G. & Tsuzuki, M. D. S. G. (2019). A review of electrical impedance tomography in lung applications: Theory and algorithms for absolute images. *Annual Reviews in Control*, *48*, 442–471. https://doi.org/10.1016/j.arcontrol.2019.05.002

[2] Reynolds, J. M. (2011). *An introduction to applied and environmental geophysics*. John Wiley & Sons.

[3] Dickin, F. J., Waterfall, R. C., Williams, R. A., Xie, C. G., Beck, M. S., Huang, S. M., llyas, O., Hoyle, B. S., Hunt, A. & Lenn, C. (1992). Tomographic imaging of industrial process equipment: techniques and applications. *IEE Proceedings G-Circuits, Devices and Systems*, *139*(1), 72–82. https://doi.org/ 10.1049/ip-g-2.1992.0013

[4] Todoroki, A., Ueda, M., & Hirano, Y. (2007). Strain and damage monitoring of CFRP laminates by means of electrical resistance measurement. *Journal of Solid Mechanics and Materials Engineering*, *1*(8), 947–974. https://doi.org/10.1299/jmmp.1.947

[5] Nonn, S., Schagerl, M., Zhao, Y., Gschossmann, S., & Kralovec, C. (2018). Application of electrical impedance tomography to an anisotropic carbon fiber-reinforced polymer composite laminate for damage localization. *Composites Science and Technology*, *160*, 231–236. https://doi.org/10.1016/j.compscitech.2018.03.031

[6] Gao, X., Wei, T., Dong, H., & Song, Y. (2019). Damage detection in 2.5 DC/SiC composites using electrical resistance tomography. *Journal of the European Ceramic Society*, *39*(13), 3583–3593. https://doi.org/10.1016/j.jeurceramsoc.2019.04.046

Metrol. Meas. Syst., Vol. 29 (2022), No. 2, pp. 347–360
DOI: 10.24425/mms.2022.140037

[7] Thomas, A. J., Kim, J. J., Tallman, T. N., & Bakis, C. E. (2019). Damage detection in self-sensing composite tubes via electrical impedance tomography. *Composites Part B: Engineering*, *177*, 107276. https://doi.org/10.1016/j.compositesb.2019.107276

[8] Gadomski, J., & Pyrzanowski, P. (2016). Experimental investigation of fatigue destruction of CFRP using the electrical resistance change method. *Measurement*, *87*, 236–245. https://doi.org/10.1016/j.measurement.2016.03.036

[9] Cagáň, J., & Michalcová, L. (2020). Impact damage detection in CFRP composite via electrical resistance tomography by means of statistical processing. *Journal of Nondestructive Evaluation*, *39*(2), 1–12. https://doi.org/10.1007/s10921-020-00677-2

[10] Pyrzanowski, P., & Olzak, M. (2013). Numerical modelling of resistance changes in symmetric CFRP composite under the influence of structure damage. *Composites Science and Technology*, *88*, 99–105. https://doi.org/10.1016/j.compscitech.2013.08.023

[11] Hallaji, M., Seppänen, A., & Pour-Ghaz, M. (2014). Electrical impedance tomography-based sensing skin for quantitative imaging of damage in concrete. *Smart Materials and Structures*, *23*(8), 085001. https://doi.org/10.1088/0964-1726/23/8/085001

[12] Dai, H., Gallo, G. J., Schumacher, T., & Thostenson, E. T. (2016). A novel methodology for spatial damage detection and imaging using a distributed carbon nanotube-based composite sensor combined with electrical impedance tomography. *Journal of Nondestructive Evaluation*, *35*(2), 1–15. https://doi.org/10.1007/s10921-016-0341-0

[13] Tallman, T. N., Gungor, S., Wang, K. W., & Bakis, C. E. (2014). Damage detection and conductivity evolution in carbon nanofiber epoxy via electrical impedance tomography. *Smart Materials and Structures*, *23*(4), 045034. https://doi.org/10.1088/0964-1726/23/4/045034

[14] Loh, K. J., Kim, J., Lynch, J. P., Kam, N. W. S., & Kotov, N. A. (2007). Multifunctional layer-by-layer carbon nanotube–polyelectrolyte thin films for strain and corrosion sensing. *Smart Materials and Structures*, *16*(2), 429–438. https://doi.org/10.1088/0964-1726/16/2/022

[15] Hou, T. C., Loh, K. J., & Lynch, J. P. (2007). Spatial conductivity mapping of carbon nanotube composite thin films by electrical impedance tomography for sensing applications. *Nanotechnology*, *18*(31), 315501. https://doi.org/10.1088/0957-4484/18/31/315501

[16] Jauhiainen, J., Pour-Ghaz, M., Valkonen, T., & Seppänen, A. (2021). Nonplanar sensing skins for structural health monitoring based on electrical resistance tomography. *Computer-Aided Civil and Infrastructure Engineering*, *36*(12), 1488–1507. https://doi.org/10.1111/mice.12689

[17] Smyl, D., Pour-Ghaz, M., & Seppänen, A. (2018). Detection and reconstruction of complex structural cracking patterns with electrical imaging. *NDT & E International*, *99*, 123–133. https://doi.org/10.1016/j.ndteint.2018.06.004

[18] Viets, C., Kaysser, S., & Schulte, K. (2014). Damage mapping of GFRP via electrical resistance measurements using nanocomposite epoxy matrix systems. *Composites Part B: Engineering*, *65*, 80–88. https://doi.org/10.1016/j.compositesb.2013.09.049

[19] Gungor, S., & Bakis, C. E. (2016). Indentation damage detection in glass/epoxy composite laminates with electrically tailored conductive nanofiller. *Journal of Intelligent Material Systems and Structures*, *27*(5), 679–688. https://doi.org/10.1177/1045389X15577644

[20] Isaac-Medina, B. K. S., Alonzo-García, A., & Avilés, F. (2019). Electrical self-sensing of impact damage in multiscale hierarchical composites with tailored location of carbon nanotube networks. *Structural Health Monitoring*, *18*(3), 806–818. https://doi.org/10.1177%2F1475921718776198

[21] Tallman, T. N., & Smyl, D. J. (2020). Structural health and condition monitoring via electrical impedance tomography in self-sensing materials: a review. *Smart Materials and Structures*, *29*(12), 123001. https://doi.org/10.1088/1361-665X/abb352

[22] Bauhofer, W., & Kovacs, J. Z. (2009). A review and analysis of electrical percolation in carbon nanotube polymer composites. *Composites Science and Technology*, *69*(10), 1486–1498. https://doi.org/10.1016/j.compscitech.2008.06.018

[23] Grossiord, N., Loos, J., van Laake, L., Maugey, M., Zakri, C., Koning, C. E., & Hart, A. J. (2008). High-Conductivity Polymer Nanocomposites Obtained by Tailoring the Characteristics of Carbon Nanotube Fillers. *Advanced Functional Materials*, *18*(20), 3226–3234. https://doi.org/10.1002/adfm.200800528

[24] Janczak, D., Słoma, M., Wróblewski, G., Młożniak, A., & Jakubowska, M. (2014). Screen-printed resistive pressure sensors containing graphene nanoplatelets and carbon nanotubes. *Sensors*, *14*(9), 17304–17312. https://doi.org/10.3390/s140917304

[25] Stepnowski, M., Janczak, D., Jakubowska, M., & Pyrzanowski, P. (2019). Detection of surface damage using resistance tomography in thin graphite layer. *Materials Today: Proceedings*, *12*(2), 484–490. https://doi.org/10.1016/j.matpr.2019.03.153

[26] Loh, K. J., Hou, T. C., Lynch, J. P., & Kotov, N. A. (2009). Carbon nanotube sensing skins for spatial strain and impact damage identification. *Journal of Nondestructive Evaluation*, *28*(1), 9–25. https://doi.org/10.1007/s10921-009-0043-y

[27] Kundu, P. K., Cohen, I. M., & Dowling, D. R. (2012). *Fluid Mechanics* (5th ed.). Elsevier Inc. https://doi.org/10.1016/C2009-0-63410-3

[28] Zienkiewicz, O., Lyness, J., & Owen, D. (1977). Three-dimensional magnetic field determination using a scalar potential – A finite element solution. *IEEE Transactions on Magnetics*, *13*(5), 1649–1656. https://doi.org/10.1109/tmag.1977.1059650

Marek Stepnowski, received the B.S. (2013) and M.S. (2016) degrees from the Warsaw University of Technology, Faculty of Power and Aeronautical Engineering. He is the PhD candidate. His scientific interests are experimental methods and their application in fault detection and load monitoring systems. Currently, he deals with the algorithm for identifying faults in thin conductive layers – the so-called sensing skin.

Daniel Janczak Ph.D., a graduate of the Faculty of Mechatronics of the Warsaw University of Technology, is a specialist in printed electronics. He deals with the development of printing paste compositions for the screen-printing technique for applications on flexible and stretchable substrates. Printed carbon composites developed by his team are used in biomedical applications of sensors and other measuring systems.

Prof. Paweł Pyrzanowski, received Ph.D. (1998), D.Sc. (2005) and the title of Professor (2020) at the Warsaw University of Technology, Faculty of Power and Aeronautical Engineering. His scientific interests concern mainly the issues related to the development of experimental methods and their application in mechanics, machine design and maintenance as well as construction of unique research stands and devices. His main research areas are the mechanics of fracture, the study of the properties and mechanisms of deterioration of composites, biomechanics. He is the author of more than 100 papers in journals and conference proceedings.

Prof. Małgorzata Jakubowska, Ph.D., D.Sc. graduated from the Warsaw University of Technology in the field of chemistry. Now she is Head of the Micro and Nanotechnology Division as well as Head of the Printed Electronics Department at the Centre of Advanced Materials and Technology of the Warsaw University of Technology. Her activities focus on thick film technology, especially thick film pastes and inks. Now she is involved in developing printed electronics, inks and pastes, printing techniques, and electronic devices such as sensors, medical sensors and coatings, elastic electrodes, etc.